ADVANCED MATERIALS INTERFACES
www.advmatinterfaces.de

Novel Composite of Nickel Thiocyanate-Based All-Inorganic Lead Bromide Perovskite Nanocrystals with Enhanced Luminescent and Stability for White Light-Emitting Diodes

*Saroj Thapa, Hongyang Zhu, Alexei Grigoriev, and Peifen Zhu**

Doping of $CsPbBr_3$ perovskite nanocrystals (PNCs) to achieve excellent material properties is accelerating due to their increasing use in optoelectronic devices. Herein, a novel composite of $CsPbBr_3$ PNCs with nickel thiocyanate $Ni(SCN)_2$ is reported, exhibiting stronger photoluminescence (PL) and more extended stability. The addition of $Ni(SCN)_2$ at different molar concentrations reduces the surface trap states of the host PNCs. Therefore, the microstrain, dislocation density, PL emission linewidth, and Urbach energy decrease, resulting in an increased photoluminescence quantum yield (PLQY) from 72% to high above 90%. When stored in the ambient atmosphere for 120 days, the PLQY of doped PNCs is maintained by more than four times compared to host PNCs. A combination of 3D-printed conversion layers containing green-, yellow-, and red-emitting doped PNCs with blue light-emitting diodes results in stable white light with superior color qualities. Hence, new composites with desired properties are developed as an alternative to conventional color phosphors.

1. Introduction

All-inorganic perovskite nanocrystals (PNCs) ($CsPbX_3$, $X = Cl^-$, Br^-, and I^-) have become one of the most exciting material systems over the past several years due to their low cost, solution processability, and excellent optoelectronic properties.[1] Therefore, these materials are used in various modern optoelectronic devices, including solar cells, light-emitting diodes (LEDs), photodetectors, lasers, single-photon sources, X-ray scintillators, and visible-light communications.[2–8] Recently, PNCs have emerged as suitable emission materials in LEDs due to their excellent optical properties such as tunable color emission, high photoluminescence quantum yield (PLQY), and narrow emission peaks.[9] In particular, the design of white LEDs (WLEDs) based on PNCs has been replacing conventional lighting systems because of their high energy efficiency, long lifetime, low-power consumption, and environmental protection.[10] Despite their promising applications, several studies indicate that PNCs undergo severe degradation when exposed to air, moisture, and light for an extended time.[11] These environmental effects lead to a significant degree of surface defects, especially at the surfaces or grain boundaries of the PNCs that mediate the trap-assisted nonradiative losses. The trap-mediated losses lead to photoluminescence (PL) quenching, structural disorder, and low stability. Therefore, passivation of the defect states helps to obtain highly luminescent PNCs, which can exhibit better luminescence properties and higher stability. Various strategies have been employed to chemically passivate surface defects of PNCs, including surface coating with silica/alumina or embedding in a polymer matrix, ligand engineering, and formation of a core-shell structure.[12–15] However, the encapsulation of PNCs in inorganic layers of silica and titania or core-shell structures deteriorates the optical performance of PNCs, which is characterized by large aggregates, broad spectra, and low PLQY.[13,16] Moreover, the applicability of PNCs blended with hydrophobic polymers such as poly(lauryl methacrylate) and polystyrene is relatively limited due to photo-oxidation of the polymers in the presence of ultraviolet (UV) light.[17] Besides, the ligand-exchange approach would still restrict the stability and structural integrity of PNCs due to the detachment of ligands during isolation, purification, and storage.

More recently, studies have suggested that doping of metal ions (B or X-site), including transition metal ions and pseudo-halide anions, positively affects the optoelectronic properties of perovskite structures.[18,19] In particular, doping can modify the energy formation, which improves the crystal quality and reduces crystal defects.[15] As a result, PNCs exhibiting higher luminescence efficiency and improved stability were obtained. The theoretical and experimental studies on Ni^{2+}-doped $CsPbX_3$ PNCs showed that Ni^{2+} doping the dopants essentially eliminates the structural defects of the PNCs due to the increased defect formation energy, improving the short-range ordering of the lattice, and providing remarkable PLQY.[20,21] Study has also shown that Zn^{2+}-doped $CsPbBr_3$ NCs exhibit dramatically higher PLQY than pristine $CsPbBr_3$ NCs without any shift in the

S. Thapa, H. Zhu, A. Grigoriev, P. Zhu
Department of Physics and Engineering Physics
The University of Tulsa
Tulsa, OK 74104, USA
E-mail: pzhu@missouri.edu
P. Zhu
Department of Electrical Engineering and Computer Science
University of Missouri
Columbia, MO 65211, USA

The ORCID identification number(s) for the author(s) of this article can be found under https://doi.org/10.1002/admi.202200710.

DOI: 10.1002/admi.202200710

 © 2022 Wiley-VCH GmbH

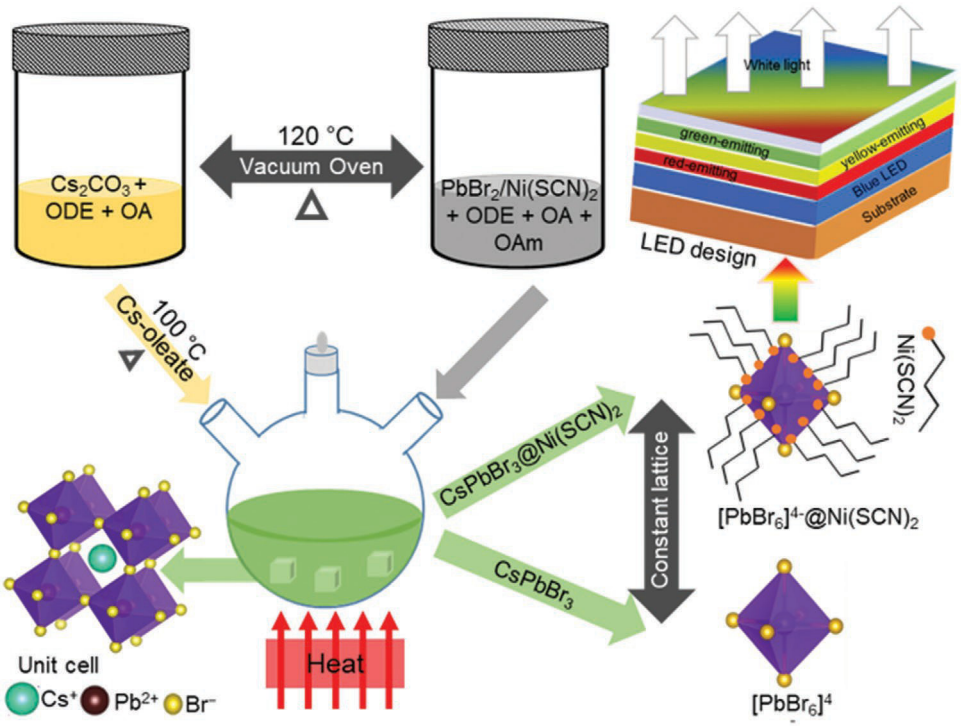

Figure 1. Schematic illustration of the comprehensive strategy, starting from the material synthesis to the device fabrication for white light emission.

emission peak. The observed effect is attributed to introducing bromide-rich conditions and the coverage of the $CsPbBr_3$ PNC surfaces with $PbBr_2$ layer due to the defect passivation.[22] Other studies showed that the introduction of thiocyanate (SCN^-) into PNCs significantly improves crystalline quality, moisture stability, and device performance.[23–26] Due to the large formation constant between Pb^{2+} and SCN^- and the enhanced passivation of under-coordinated Pb^{2+} ions, the SCN^--based metal halide perovskites exhibit a highly luminescent and chemically stable perovskite structure.[25] Despite the high popularity of each dopant on its own, no study has reported the simultaneous doping of Ni^{2+} and no study has reported the simultaneous doping of Ni^{2+} and SCN^- in a PNC sample. This motivates us to investigate how the choice of this combination would entail a change in the photophysical properties of the $CsPbX_3$ PNCs. Very recently, the strategy of using inorganic passivation has proven to be extremely successful in improving both the optical stability and device performance of $CsPbX_3$ PNCs.[27] Nevertheless, it remains an attractive goal to identify efficient inorganic salts that can impart the desired physical and chemical properties to PNCs and increase the stability of the inherent material.

In this work, we have developed a novel composite system that improves the luminescence properties and stability of $CsPbBr_3$ PNCs. As-synthesized PNCs demonstrate an immense potential for the development of efficient illumination devices (**Figure 1**). For the novel composite system, we introduce nickel thiocyanate [Ni(SCN)$_2$] as a dopant in the synthesis of $CsPbBr_3$ PNCs. And we studied the change in structural, morphological, and optical properties of $CsPbBr_3$ PNCs for the different molar concentrations of dopants. Ni(SCN)$_2$ added $CsPbBr_3$ PNCs are synthesized by the conventional hot-injection method (explained in detail in supporting information) with slight modifications (schematically shown in Figure 1).[4,28] The dopant effectively modifies the surface trap states in the as-synthesized PNCs without affecting their crystal structure and morphology. We expect that the dopant is implanted on the surface of the host PNCs, which has a remarkable effect on the optical properties of as-synthesized PNCs. As-prepared nanocube-shaped PNCs exhibited size-tunable bandgap energy and PL emission spectra with a narrower full width at half maximum (FWHM). The FWHM of PL emission and Urbach energy decreases with an increasing concentration of dopants. As a result, the PLQY increases from 72% to 92%. Besides utilizing the anion exchange reaction technique, the bright PL emission is tuned over the entire visible spectral range. Compared to the host PNCs, the Ni(SCN)$_2$-based PNCs maintained high PLQY (above 90%), preserving the original emission profile with a minimal fluctuation in the peak position and the corresponding FWHM of PL emission when exposed to an ambient atmosphere for more than 120 days. This attribute confirms the excellent luminescence stability, which helps design stable WLEDs. Therefore, the 3D printed color conversion layers containing green, yellow, and red-emitting doped PNCs were combined with blue LED chips to fabricate WLED. The WLED exhibits superior color quality, excellent vision performance, and high color stability. The experimental results have shown great potential for using similar PNCs for efficient lighting and display practically.

2. Results and Discussion

The crystalline structure of the $CsPbBr_3$ NCs with different Ni(SCN)$_2$ (0–50%) concentrations was determined from the

© 2022 Wiley-VCH GmbH

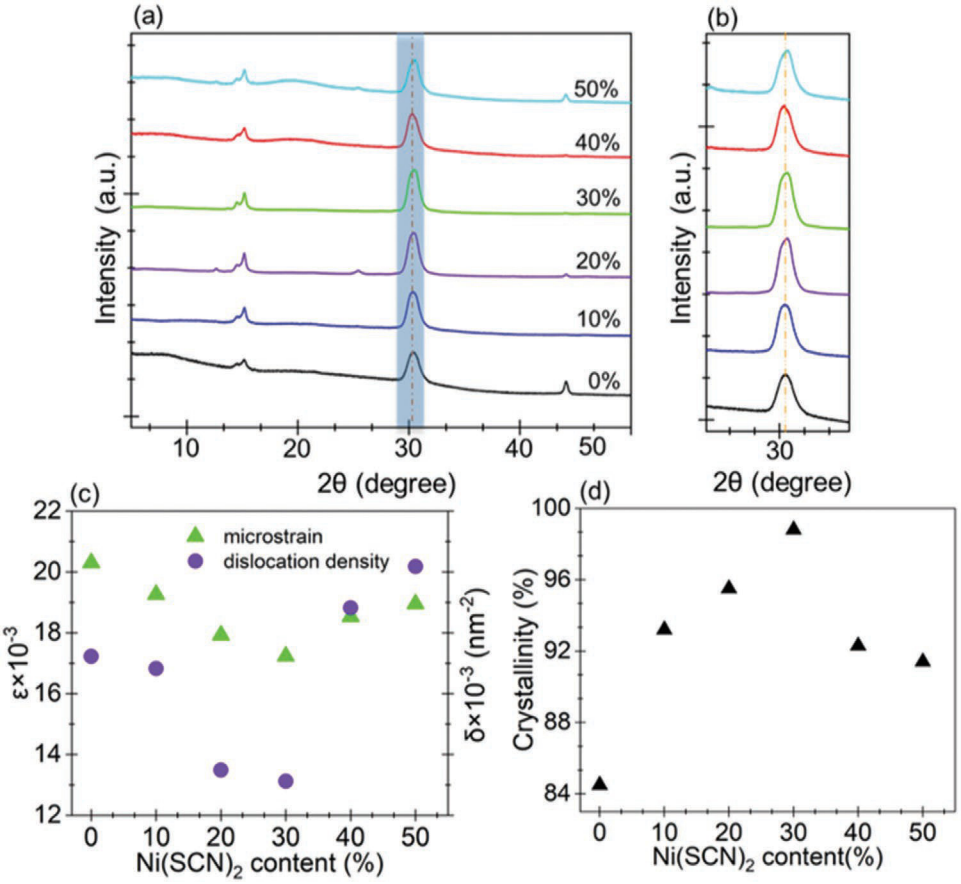

Figure 2. a) XRD patterns and b) enlargement of (200) diffraction plane of $Ni(SCN)_2$ added $CsPbBr_3$ PNCs. The variation of c) microstrain and dislocation density and d) crystallinity as a function of the concentration of $Ni(SCN)_2$ of as-synthesized PNCs.

X-ray diffractometer (XRD) spectra, as shown in **Figure 2**a. The XRD spectra consist of prominent diffraction peaks at ≈15° and 30° that correspond to the (100) and (200) diffraction planes with a d-spacing of 0.29 Å for the (200) plane, confirming the cubic structure of the $CsPbBr_3$ PNCs.[29] At a different concentration of $Ni(SCN)_2$, the diffraction peaks are identical, indicating that crystal growth in the PNCs is not structurally affected by the addition of $Ni(SCN)_2$. The XRD spectra further reveal no new diffraction peaks upon the addition of $Ni(SCN)_2$, indicating no impure crystal phase is induced. We could not detect any explicit shift in the diffraction peak position (Figure 2b) and the d-spacing, confirming the absence of homogeneous strain within the lattice.[29,30] Possibly, the substantial mismatches between the ionic radii and the electronegativities of different ions present in $Ni(SCN)_2$ are responsible for the unchanged diffraction peak position.[20,31] Besides, the nominal content of dopants entering into the perovskite lattice is expected to unalter the diffraction peak position. Under the circumstances, the dopants are likely to be expelled onto the surface and grain boundaries of perovskites.[29] The likelihood of surface implantation of dopants can be corroborated by the decreasing trend in microstrain (ε) of as-synthesized PNCs (**Table 1** and Figure 2c). Furthermore, the decreasing microstrain results in a relaxation of the perovskite lattice, leaving the perovskite crystal structure

Table 1. Estimation of diffraction peak width, microstrain, dislocation density, and crystallinity of $CsPbBr_3$ PNCs at a different molar concentration of $Ni(SCN)_2$.

$Ni(SCN)_2$ [%]	β [°]	$\varepsilon \times 10^{-3}$	$\delta \times 10^{-3}$ [nm^{-2}]	Crystallinity [%]
0	1.2631	20.3	17.22	84.53
10	1.1978	19.26	16.82	93.15
20	1.1159	17.92	13.49	95.52
30	1.0774	17.23	13.12	98.87
40	1.1528	18.53	18.82	92.34
50	1.1779	18.95	20.18	91.47

© 2022 Wiley-VCH GmbH

and the diffraction peak position unchanged. In particular, the microstrain explains the imperfections within crystal structures, including structural disorder, dislocations, vacancies, stacking faults, and interstitials.[32] Following the microstrain variation, the estimated value decreases from ≈20.30 × 10^{-3} to ≈17.23 × 10^{-3} for 0–30% of $Ni(SCN)_2$ and increases to ≈18.95 × 10^{-3} at 50% $Ni(SCN)_2$. Furthermore, we found a similar trend in the variation of other structural parameters, including the diffraction peak width (β), dislocation density (δ), and crystallinity (Table 1). In brief, the structural parameters decrease with an increase in the concentration of dopants up to 30% and then increase for the higher doping concentrations. A dopant concentration of 30% indicates the limit to the concentration of $Ni(SCN)_2$ which the PNCs tolerate before any negative impact on the structural properties occurs, referred to as critical doping concentration. As shown in Table 1, the diffraction peak width decreases from 1.2631 to 1.0774 for 0–30% but increases to 1.1779 for 50% of $Ni(SCN)_2$. A decrease in stacking faults and structural disorder decreases the width of the diffraction peak.[30] Figure 2c shows that the dislocation density decreases from ≈17.22 × 10^{-3} nm^{-2} to 13.12 × 10^{-3} nm^{-2} up to a critical doping concentration and then increases to 20.18 × 10^{-3} nm^{-2} for the highest doping concentration. The decrease in microstrain and dislocation density indicates reduced surface trap states, which are desirable for higher luminescence properties and device performance.[30,33] Favored by these defect modifications, the crystallinity of the PNCs increases with an increase in the $Ni(SCN)_2$ content up to a critical doping concentration. Depending on the concentrations of $Ni(SCN)_2$, the crystallinity of the PNCs varies from ≈98.87% to 84.53% (Table 1). This variation is well indicated in Figure 2d. The crystallization pattern change is expected to influence the crystal growth by altering the crystal growth energy in the presence of $Ni(SCN)_2$.[34]

To understand the effects of $Ni(SCN)_2$ on the shape and size variation of $CsPbBr_3$, we analyzed transmission electron microscopy (TEM images, **Figure 3**a). The TEM images of as-synthesized PNCs show nearly cubic morphology regardless of the dopant concentrations. Although the shape of the PNCs is identical, we noticed a disparity in the size of the PNCs, which is shown in Figure 3b. The average edge length of $Ni(SCN)_2$ added $CsPbBr_3$ PNCs increases up to a critical doping concentration (30%, ≈8.74 ± 0.14 nm) when compared to the $CsPbBr_3$ PNCs host (≈7.62 ± 0.05 nm), respectively. Whereas the corresponding mean size of the PNCs decreases to ≈7.29 ± 0.07 nm and ≈7.04 ± 0.09 nm for the higher doping concentration of 40% and 50%, respectively. The substantial decrement of microstrain up to a critical doping concentration slows down crystallization by adsorbing the impurity ions to the crystal surfaces resulting in the expansion of dimensions. Furthermore, the expansion of PNCs can be attributed to the better passivation of the $Ni(SCN)_2$ added $CsPbBr_3$ PNCs surface by the X-type bonding of the dopant, since the presence of sulfur anions causes an enhanced interaction to the metal atoms of both the PNCs surface and the subsequent metal salt.[35] The sudden decrease in the dimension of the PNCs is expected due to the increased non-uniform microstrain within the PNCs that are responsible for decreasing the crystal growth.[34] The variation of the average dimensions of PNCs is shown in Figure 3b, which is estimated from the distribution statistics shown in Figure 3c. Figure 3c further demonstrates the narrower distribution of the PNCs with a squareness of 0.9 ± 0.01.

To better understand the fluorescence properties, we examined the PL emission and absorption spectra of the PNCs solution (**Figure 4**). The PL emission spectra of $CsPbBr_3$ PNCs at different molar concentrations of $Ni(SCN)_2$ were recorded at an excitation wavelength of 365 nm (Figure 4a). The PL emission spectrum of as-grown PNCs shows a sharp excitonic emission peak with a tunable emission peak wavelength (≈512.0–520.5 nm), which is shown in **Table 2**. On increasing the dopant concentration from 0–30%, the emission peak wavelength gets red-shifted, extending from ≈514.4 nm to ≈520.5 nm. However, for the higher doping concentration (40–50%), the corresponding wavelength peak receives a blue shift. The spectral shift in PL emission peak is attributed to the strain-dependent change in dimension of the PNCs during doping. Furthermore, this shifting phenomenon is an indication of the weak effect of $Ni(SCN)_2$ on the electronic structure of the host PNCs at their higher concentration. As-grown PNCs depict the narrow FWHM, ranging from ≈17.7 to ≈19.6 nm (Table 2). FWHM of PL emission first decreases up to a critical doping concentration and then increases with a further increase in dopants. The decreased FWHM of PL emission for doped NCs is related to the uniform size distribution of NCs. The decreasing emission linewidth indicates the reduced trap states, proving the fluorescence is of high color purity and saturated. However, the broadening of the PL line shape beyond the critical doping concentrations is associated with a higher energetic disorder due to the reduced crystallinity or electron-phonon coupling changes.[36] We note that no new absorption bands are introduced by doping (Figure 4b). The UV-vis absorption peak of PNCs shifts first to a higher and then to a lower wavelength with increasing doping concentration, evidencing the weak effect of doping on the electronic structure of the host PNCs. The corresponding absorption spectra are used to calculate the bandgap energy of the material (Table 2). When the dopant concentration increases from 0% to 30%, the measured band gap energy decreases from ≈2.56 to ≈2.45 eV, probably due to the shift of the valence band minimum towards the Fermi energy level compared to the $CsPbBr_3$ PNCs.[29] However, the bandgap energy widens to ≈2. 49 eV as the doping concentration increases to 50%, which can be ascribed to the weak quantum confinement effect. The variation of this bandgap energy is presented in Figure 4c. In addition, the Urbach energy, characterizing the structural defects and the degree of crystallinity in the structure, is estimated using the spectra (Figure S1a, Supporting Information) and presented in Table 2.[37] The Urbach energy decreases from ≈2.37 to ≈2.29 eV with increasing $Ni(SCN)_2$. It is anticipated that the improved structural ordering of PNCs causes a decrease in the Urbach energy. This ultimately leads to fewer trap states, and trap-assisted recombination rates, resulting in improved luminescence properties. Therefore, the PLQY of the host NCs significantly increases from ≈72% to 92% for increasing dopant concentration (Table 2). The variation of dopant concentration-dependent PLQY is shown in Figure 4d. For a given halide perovskite structure, Ni^{2+} ions as a dopant have a strong preference for octahedral coordination with the surrounding anions. Therefore, the presence of Ni^{2+} ions during the synthesis approach appears to compensate for radiative losses due to the

© 2022 Wiley-VCH GmbH

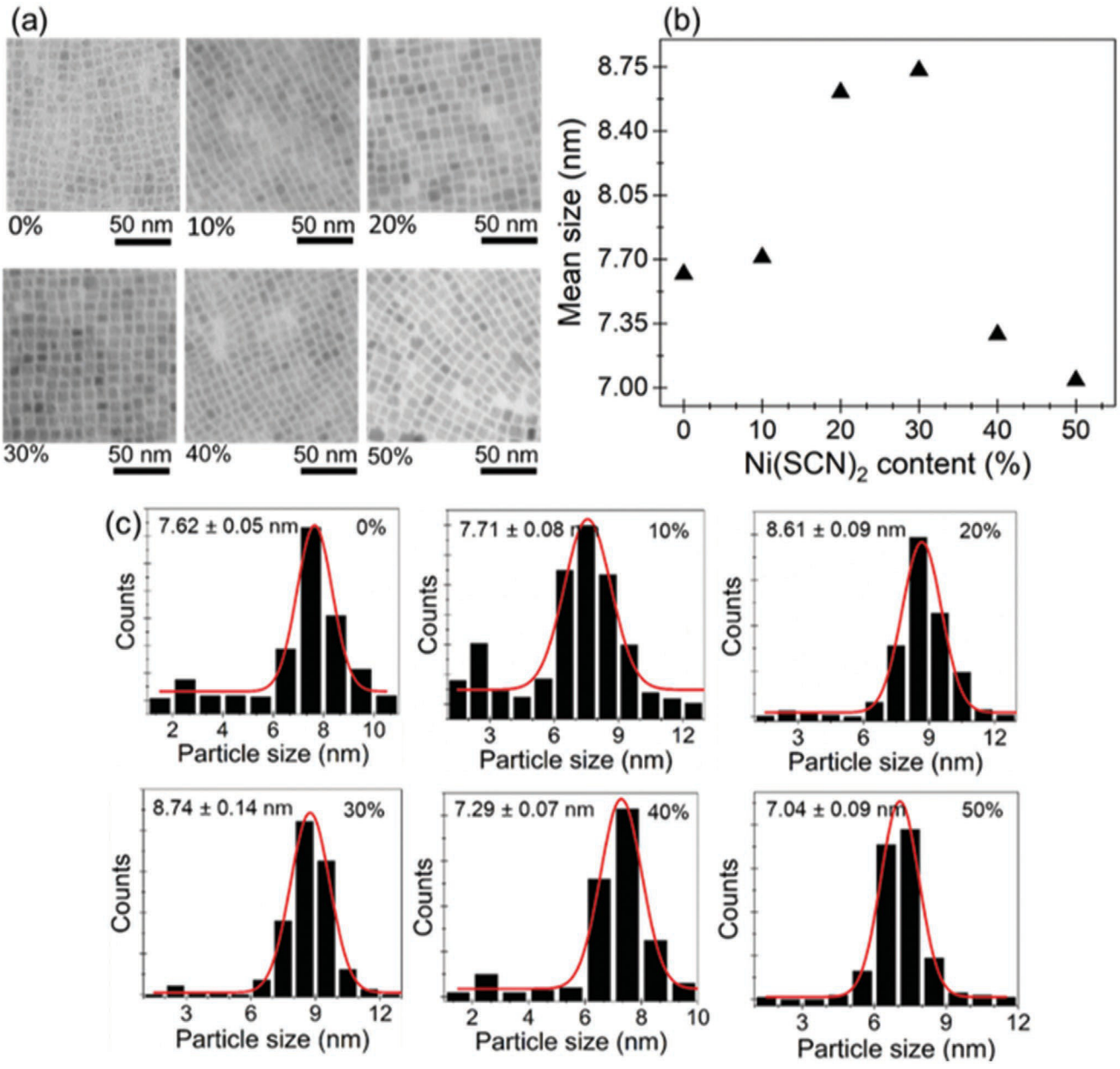

Figure 3. a) TEM images, b) variation of mean particle size as a function of the concentration of $Ni(SCN)_2$, and c) histogram of the particle size distribution of as-synthesized PNCs.

trap states, most likely by enhancing the short-range order of the crystal lattice. This further reduces the formation energies of the Ni^{2+} halide bands compared to the formation energy of the Pb^{2+} halides, therefore, providing larger octahedron stability and reducing the generation of non-radiative metal vacancies.[20,21] The approach to treating the as-synthesized PNCs at the same time using the SCN^- ions are expected to generate more robust bonds to Ni^{2+} (favored octahedral coordination) than Pb^{2+} halide bonds and possess nonspherical structures, which are geometrically immobilized by the surrounding lattice. Furthermore, the introduction of SCN^- in $CsPbBr_3$ PNCs suppresses the shallow trap states within the surface of PNCs that coordinate the under-coordinated lead atoms on the surface of PNCs.[20,23] Given the advantages of Ni^{2+} and SCN^- in $CsPbBr_3$ PNCs, our experimental results confirm that $Ni(SCN)_2$ helps increase the PLQY of $CsPbBr_3$ PNCs. However, the unusual decrease in PLQY for the highest doping concentration might be due to excessive $Ni(SCN)_2$ passivating the crystal lattice introducing new defects. The PL excitation spectra were measured at the corresponding peak emission wavelength (Figure S1b, Supporting Information). The shape of the spectrum is almost identical and independent of the $Ni(SCN)_2$ concentration. The broadband excitation spectra of as-grown NCs range from 260 to 480 nm, suggesting that these NCs can serve as efficient photons down-conversion phosphors in conjunction with III-nitride UV/blue LEDs.

© 2022 Wiley-VCH GmbH

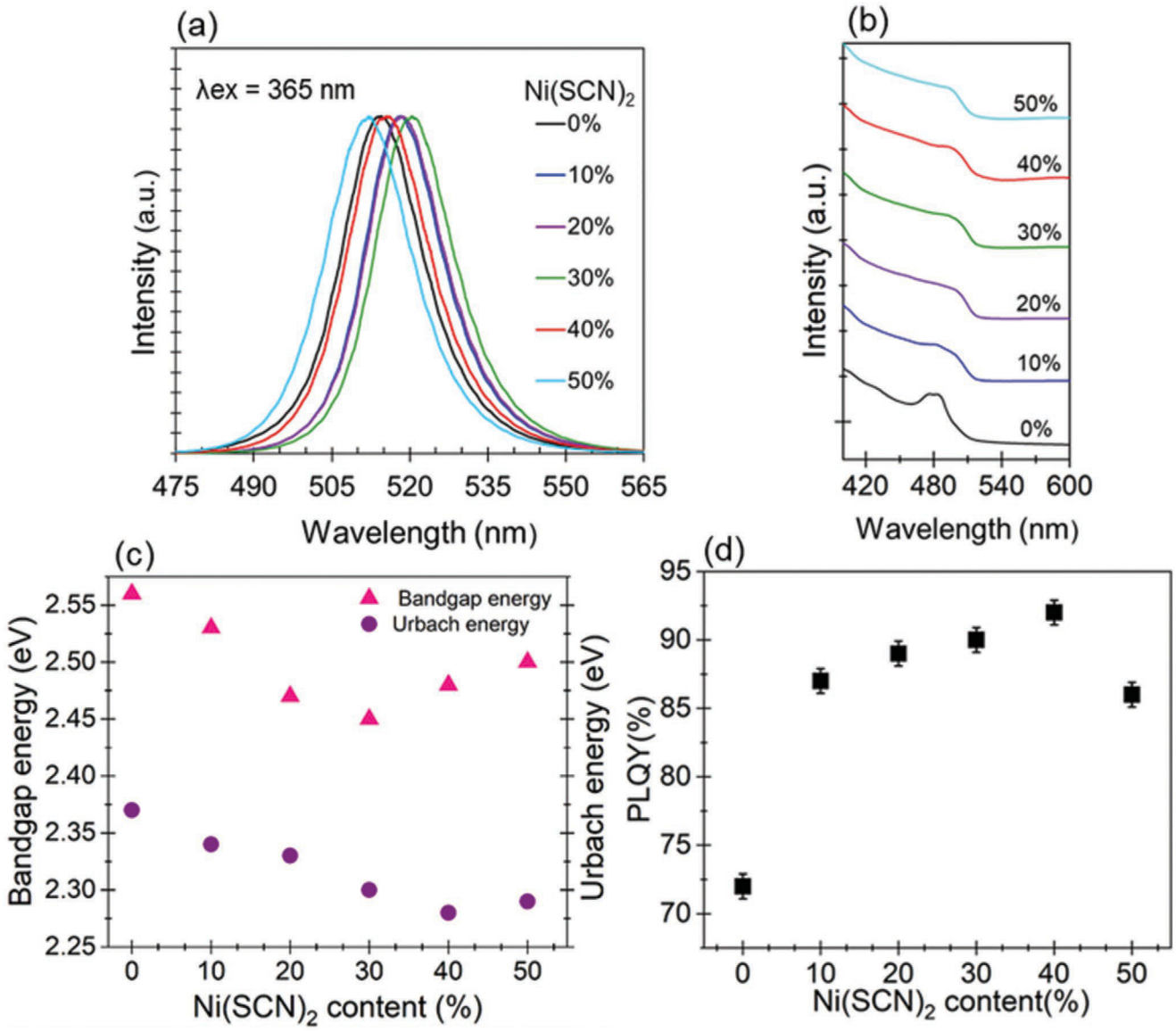

Figure 4. a) PL emission, b) UV-vis absorption spectra of $CsPbBr_3$ PNCs synthesized at a different concentration of $Ni(SCN)_2$. The variation of c) bandgap and Urbach energy, and d) PLQY (fitted with an error bar) as a function of the concentration of $Ni(SCN)_2$ of as-synthesized PNCs.

The instability of the metal halide PNCs impedes the commercial development of these materials. The investigation of the stability of PNCs toward ambient air and moisture is another crucial issue to evaluate its quality. Therefore, we tested the PL properties (**Figure 5** and Figure S3, Supporting Information) of as-synthesized PNCs when stored in an

Table 2. Estimation of PL emission peak, PL FWHM, bandgap energy, Urbach energy, and PLQY of $Ni(SCN)_2$ added $CsPbBr_3$ NCs at a different molar concentration of $Ni(SCN)_2$.

$Ni(SCN)_2$ [%]	PL peak [nm]	FWHM [nm]	Bandgap energy [eV]	Urbach energy [eV]	PLQY [%]
0	514.4	18.5	2.56	2.37	72
10	518.0	17.7	2.53	2.34	87
20	519.4	17.8	2.47	2.33	90
30	520.5	18.0	2.45	2.30	90
40	515.6	18.7	2.48	2.28	92
50	512.0	19.6	2.50	2.29	91

© 2022 Wiley-VCH GmbH

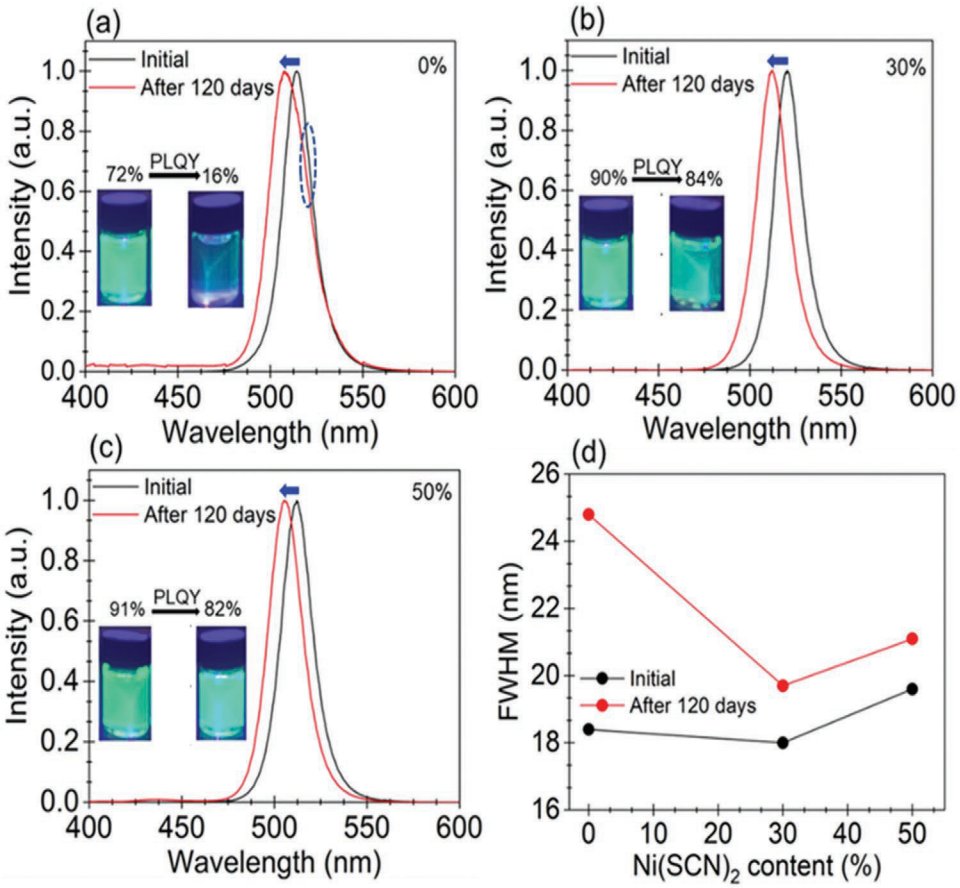

Figure 5. PL emission of fresh and aged samples (over 120 days) that were prepared at a) 0%, b) 30%, and c) 50% $Ni(SCN)_2$, respectively (inset is the photograph of colloidal solution). d) Variation of corresponding FWHM of PL emission as a function of the concentration of $Ni(SCN)_2$. The "initial" indicates the freshly prepared samples.

ambient atmosphere for more than 120 days without encapsulation. Over 120 days, the PL emission profile (Figure 5a,b,c) exhibits a narrower linewidth and single-peaked emission spectra with a blue shift in peak position (Table S1, Supporting Information). The shift in the emission peak can be attributed to the shrinkage of the PNCs, which is consistent with TEM images (Figure S2, Supporting Information). After prolonged exposure of PNCs to the open air, water (H_2O) molecules from the moisture might have been absorbed on the surface of PNCs. When these H_2O molecules dissociate into H_3O^+ and OH^- ions, the interaction between PNCs and capping ligands is enhanced, reducing the dimensions of PNCs.[38,39] For the $CsPbBr_3$ PNCs, we observe a distortion in the emission peak profile (Figure 5a, marked by the circle), indicating the formation of PNCs of different sizes due to the degradation of the PNCs. The TEM images (Figure S2, Supporting Information) corresponding to $CsPbBr_3$ PNCs depict a higher concentration of cube-shaped particles with average dimensions ≈of 4.46 ± 0.05 nm and fewer concentrations of circular particles with average sizes ≈of 22.40 ± 2.5 nm. The narrower linewidth as a function of dopant concentration (Figure 5d) shows that the FWHM corresponding to $CsPbBr_3$ PNCs increases remarkably from ≈18.5 to ≈24.8 nm, confirming an increase in the concentrations of defects. However, a smaller drift in PL FWHM (<2nm, Figure 5d) of $Ni(SCN)_2$-based PNCs compared to $CsPbBr_3$ suggests the reduced defect concentration within the PNCs due to the $Ni(SCN)_2$-passivation effect. Variation in defect concentrations results in a considerable change in PLQY over time, as indicated by the time-dependent PLQY plot in Figure S3, Supporting Information. The PLQY of $CsPbBr_3$ PNCs drops sharply to nearly 25% after 50 days of storage and then gradually levels off. The decreasing trend in PLQY continues until PNCs maintain almost 16% of their initial measurement. In contrast, PLQY of $Ni(SCN)_2$ added $CsPbBr_3$ PNCs marginally decreases over time and exceptionally contain more than 90% of the initial PLQY after 120 days of storage. Thus, $Ni(SCN)_2$-based perovskites exhibit stronger resistance against air, moisture, water, and oxygen. The experimental observation is further supported by the change in intensity of the color emission of the corresponding colloidal solution photographed under UV light of 365 nm (inset of Figure 5). The stronger green emission of freshly prepared $CsPbBr_3$ PNCs quenches, changing the emission color to faint green emission over time. However, the colloidal solution of $Ni(SCN)_2$ added $CsPbBr_3$ PNCs more or less retained their initial emission colors, suggesting the luminesce stability of the PNCs. Due to the better passivation effect of defect regions in the presence of $Ni(SCN)_2$, $Ni(SCN)_2$-based PNCs

© 2022 Wiley-VCH GmbH

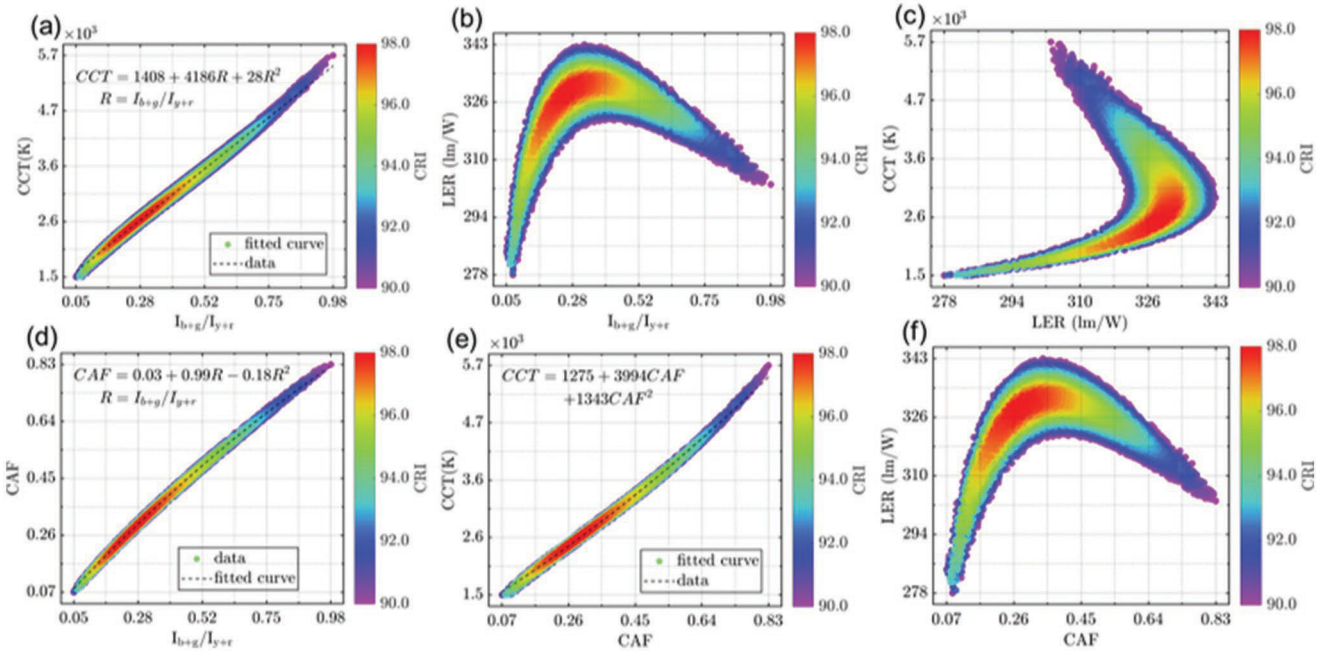

Figure 6. a) CCT and b) LER as a function of power ratio of different color combinations. c) LER as a function of CCT, d) CAF as a function of the power ratio of different color combinations, e) CCT as a function of CAF, and f) LER as a function of CAF. The color bar indicates the corresponding CRI.

might impede the penetration of water molecules because the defect-rich regions of the PNCs, bounded to surface boundaries, infiltrate the moisture.[38,39] Therefore, the better stability and outgoing performance can be ascribed to the constraint of the dynamic surface due to the elimination of the defect states prone to the non-radiative recombination phenomenon and the stronger bonding interaction in the presence of $Ni^{2+}$and SCN^{-}. To investigate the potential application of these materials in photon down-converted WLED, we first optimize the optical performance of the WLED structure of the form shown in Figure 1. In brief, the device configuration consists of green, yellow, and red-emitting PNCs, which is optically pumped with a blue LED chip. The spectral power distributions (SPDs) for white light are then generated by tuning the ratio of green, yellow, and red-emitting NCs normalized with respect to the blue emission of the LED chip. The SPD analysis (discussed in detail in the Supporting Information) for white light was optimized by characterizing the different performance characteristics for good color quality and high vision performance, including correlated color temperature (CCT), luminous efficacy of radiation (LER), and circadian action factor (CAF), as shown in **Figure 6**. Our theoretical results show that we can design white light with high color rendering index (CRI, maximized up to 97), high LER (up to 330 lm W^{-1}), and tunable CCT (2141–5749 K) by choosing the appropriate ratios of the different emissions. CRI is a metric that measures the ability of a light source to reproduce the colors of the illuminated object accurately. CRI values that are 90 and above are considered excellent for indoor lighting applications.[40] The color characteristics of seven representative white LEDs with different CCT are summarized in Table S2, Supporting Information. The International Commission on Illumination (CIE) color coordinates of these white LEDs for different CCTs are close to the Planckian locus (Figure S4). The closeness of these color coordinates is represented by a small positive D_{uv} (0.00001–0.0009), indicating that the color temperature we determined is preferred for brightness, comfort, and chromaticity. The CCT of a light source is defined as the blackbody's temperature of the closest chromaticity and corresponds to the feeling of how "warm or cold" a light source is. The dependence of CCT on the ratios of the sum of blue and green emissions to the sum of yellow and red emissions (Figure 6a) depicts a linear trend in variation that satisfies the fitted functions of the form:

$$\mathrm{CCT}(\mathcal{R}) = 1408 + 4186\mathcal{R} + 28\mathcal{R}^2 \quad (1)$$

where R is the ratio of the sum of the blue and green emissions to yellow and red emissions. This figure represents that the CCT of white light increases as the value of R increases. Low values of R result in a warm white light (low CCT) with a high CRI, while high R values result in a cool hue (high CCT) with a low CRI. The dependence of LER on R defines the effectiveness with which a given SPD stimulates the sensitivity of human vision. As shown in Figure 6b, varying the value of R affects the LER of the device configuration such that LER (as high as 300 lm W^{-1}) increases by increasing the yellow and red emissions or decreasing the blue and green emissions, or by simultaneously increasing yellow, and red emissions and decreasing the blue, and green emissions, which helps in maximizing the vision performance and vice versa. The LER above 300 lm W^{-1} demonstrates the high vision performance of WLEDs.[41] Thus, the estimation of LER for a given SPD examines the vision performance of white light. This enhanced vision performance

© 2022 Wiley-VCH GmbH

of white emission results in warm light (low CCT, Figure 6a). Conversely, Figures 6a and b represent that a decreasing trend in the vision performance is expected to generate cool white light (high CCT). An increase in CCT increases the sensation of brightness; however, increased CCT does not linearly increase lighting comfort due to the reducing vision performance of the emitted light (Figure 6c). As the color temperature increases, LER values corresponding all descend with a decreasing trend in CRI (Figure 6c). The calculation of CAF studies the effect of emitted white light on human health. CAF is another figure of merit which refers to the biological action per unit of visual response. CAF impacts hormone production (melatonin secretion), sleep-wake cycles, body temperature regulation, and alertness related to human health. Different CAF values are advisable depending on the time of day. For the same luminance, white light with low CAF is desirable at night, while a high CAF improves the working efficiency during the day.[42] A high CAF value indicates that the light source can concentrate the energy in a spectral region that is circadian-sensitive, thus having a strong impact on human health. CAF does have a positive correlation with alertness, the higher the CAF of lighting, the more it can enhance alertness. A tunable CAF as a function of R is generated by fitting the equation of the form:

$$\mathrm{CAF}(\mathcal{R}) = 0.03 + 0.99\mathcal{R} - 0.18\mathcal{R}^2 \quad (2)$$

which is shown in Figure 6d. The graph illustrates almost a linear relationship between CAF and *R,* a trend similar to the variation of CCT as a function of *R*. As CCT decreases, the blue content of SPD decreases, leading to an increase in the minimum attainable CAF (Figure 6e).[43] Thus, the samples with low and high CCTs were tuned to obtain a wide circadian variability. In comparison to CCT, CAF seems to be a better index for the alertness-promoting effect of light. Figure 6f depicts calculated CAFs versus LERs. With the increasing CAF, LER gradually increases to a critical value and then decreases after that, where the CRI corresponding to it also changes accordingly. Thus, a light source with high LER, high CRI, and low CAF is preferred for efficient lighting applications.

Furthermore, to demonstrate the practical utility of $Ni(SCN)_2$ added $CsPbBr_3$ PNCs, we experimentally fabricated a WLED by combining green, yellow, and red-emitting color conversion layers with a blue InGaN blue chip (discussed in detail in Supporting Information). To the best of our knowledge, this is the first report that demonstrates the generation of white light using the composite of $Ni(SCN)_2$ contained $CsPbX_3$ PNCs. For the preparation of yellow and red-emitting PNCs, we modulated the composition of Br^-/I^-, containing 30% $Ni(SCN)_2$ because $CsPbBr_3$ PNCs at 30% $Ni(SCN)_2$ exhibited the least defect states, highest crystallinity, and narrowest emission linewidth with high PLQY. When the ratio of Br^- to I^- decreases, the PL emission peak extends from the green to red wavelength region. The structural, morphological, and optical properties of the yellow and red-emitting PNCs are shown in Figure S5, Supporting Information. The XRD scan (Figure S5a, Supporting Information) corresponding to these PNCs confirms the cubic structure marked with lattice expansion.

Moreover, the corresponding PNCs show the cubic morphology with an increase in dimensions (inset of Figure S5a, Supporting Information). The corresponding PL emission (Figure S5b, Supporting Information) peak wavelength is centered at ≈571.2 and ≈631.8 nm with a corresponding narrower linewidth of ≈39 and ≈41 nm, and bandgap energy of ≈2.05 and ≈1.96 eV, which is desirable for the fabrication of WLEDs. For the fabrication of WLED, a thin layer of the 3D-printed conversion layers (discussed in detail in Supporting Information) was separately coated with the green, yellow, and red-emitting PNCs with wavelengths ≈520.5, ≈571.2, and ≈631.8 nm, respectively, and act as color conversion layers for generating white light. The 3D printed thin structures have an estimated thickness of 0.15 mm which is thinner than the glass/quartz substrates. The printed structure is based on a plastic material (polylactic acid) with a low value of the refractive index (≈1.46) that helps in reducing the material cost and the excess photon loss during the WLED design. Structurally, the printed structure has multiple rectilinear channel-like structures, allowing the formation of homogeneously distributed thin films upon drop-casting the colloidal solution of PNCs on the top of it. Thus, the designed structure is expected to reduce the coffee ring effect, unlike the spin-coated films that prompt the lighting output. In addition, to eliminate the undesirable effect of anion exchange during the device fabrication consisting of perovskite layers with different anion compositions and retaining their fluorescence property, we consider preparing the 3D printed color conversion layer. The three different color conversion layers were stacked one above the other in the hierarchy of decreasing bandgap energy on the top of a blue LED chip operating at 5.05 mA and 7.5 V with an emission peak centered at 460 nm. The electroluminescence (EL) spectrum (**Figure 7**a) of the working WLED (inset of Figure 7a) shows four emission peaks assigned to the blue LED chip and the green, yellow, and red-emitting NCs. The presence of distinct emission peaks in the EL spectra indicates the omission of the anion exchange reaction between the different emitting layers. Under the current of 5.05 mA, the WLED features a high LER of 329 lm W^{-1}, a high CRI of 90, CCT of 5242 K, and the CIE coordinates (0.34, 0.33) close to the standard white light.[44] The estimated CIE coordinates (Figure 7b) are close to the Planckian locus ($D_{uv} < 0.013$), which demonstrates an excellent color saturation that is comfortable for human vision. These properties suggest good prospects for these materials as a replacement for conventional rare-earth-doped phosphors in next-generation WLEDs. The EL spectra of the WLEDs (Figure S6a, Supporting Information) were examined under the operating current (ranging from 5.05 to 45.05 mA) to evaluate the color stability of the device. The corresponding changes in CRI, CCT, LER, and CIE coordinates are summarized in Table S3, Supporting Information. Figure S6b, Supporting Information demonstrates the variation in both CCT and CRI when the current is increased from 5.05 to 45.05 mA. For the increasing current, CCT increases from 5242 to 6670 K, while the corresponding CRI decreases from 90 to 85. In addition, the LER drops from 334 to 313 lm W^{-1}. The decrease in LER is due to the thermal degradation of PNCs when they are used to generate white light.[45] The corresponding CIE color coordinates are slightly blue-shifted from (0.340, 0.335) to (0.309, 0.331) due to the increased emission energy and device surface temperature.[46] These results demonstrate that the WLED has excellent color stability.

© 2022 Wiley-VCH GmbH

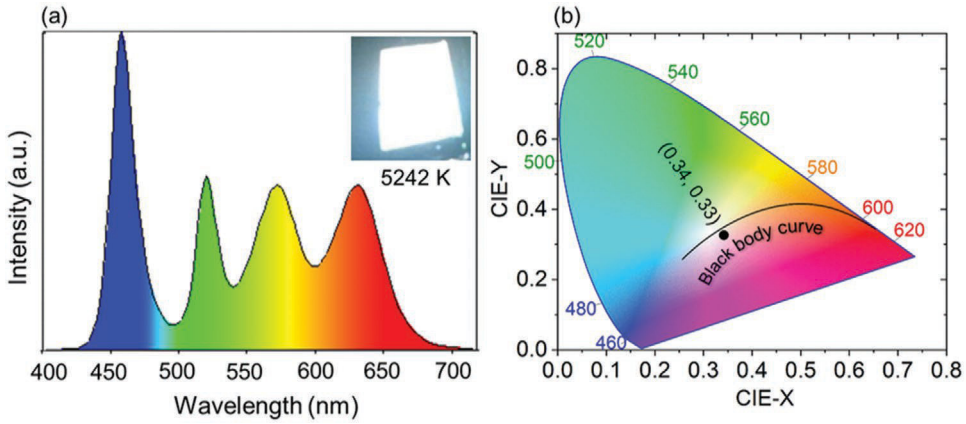

Figure 7. a) EL spectra of a WLED as a function of wavelength (inset is the working WLED with a CCT of 5242 K), and b) CIE chart showing the CIE color coordinates of a white light close to the blackbody curve (or Planckian locus).

3. Conclusion

In summary, we have synthesized $Ni(SCN)_2$ added $CsPbBr_3$ PNCs demonstrating that $Ni(SCN)_2$ as a dopant can be a novel approach that imparts superior luminescent properties and excellent PL stability against air and moisture. The dopants are likely to reside at the PNCs surface resulting in changing the optical properties while leaving the structural and morphological properties unchanged. As a result, PNCs exhibited fewer defect concentrations, which are confirmed by reducing microstrain, dislocation density, PL emission linewidth, and Urbach energy but increasing crystallinity. Moreover, due to the much-reduced defects in PNCs, the obtained $Ni(SCN)_2$-based PNCs preserve their initial PL emission profile and PL intensity as high as ≈90% after 120 days of storage, confirming the stability of the PNCs. The defect passivated $Ni(SCN)_2$-based PNCs, exhibiting green, yellow, and red emission PNCs were used as a color conversion layer in WLED fabrication. The device configuration results in a stable bright neutral white light with outstanding CRI and LER, suitable for indoor lighting. Thus, our experimental findings demonstrate that the implication of a transition metal ion combined with a thiocyanate ion in the synthesis of PNCs can be a novel and facile route for improving the optical properties and the stability of the PNCs.

Supporting Information

Supporting Information is available from the Wiley Online Library or from the author.

Acknowledgements

This work was supported by the National Science Foundation (NSF) under Award No. 1945558. The authors would like to acknowledge Professor Parameswar Harikumar's help with absorption measurements and Gopi Adhikari's help with sample preparation.

Conflict of Interest

The authors declare no conflict of interest.

Data Availability Statement

Research data are not shared.

Keywords

high quantum yield, long-term stability of perovskite nanocrystals, $Ni(SCN)_2$ added $CsPbBr_3$ PNCs, reduced trap states, white LEDs

Received: March 29, 2022
Revised: May 4, 2022
Published online:

[1] L. P. V. Kovalenko, M. I. Bodnarchuk, *Science* **2017**, *358*, 745.
[2] A. Kojima, K. Teshima, Y. Shirai, T. Miyasaka, *J. Am. Chem. Soc.* **2009**, *131*, 6050.
[3] R. , X. Y. Chin, B. Damodaran, T. J. N. Hooper, S. Mhaisalkar, N. Mathews, *ACS Appl. Nano Mater.* **2020**, *3*, 6089.
[4] L. Protesescu, S. Yakunin, M. I. Bodnarchuk, F. Krieg, R. Caputo, C. H. Hendon, R. X. Yang, A. Walsh, M. V. Kovalenko, *Nano Lett.* **2015**, *15*, 3692.
[5] J. Deng, J. Li, Z. Yang, M. Wang, *J. Mater. Chem. C* **2019**, *7*, 12415.
[6] M. M. Stylianakis, T. Maksudov, A. Panagiotopoulos, G. Kakavelakis, K. Petridis, *Materials (Basel)* **2019**, *12*, 859.
[7] I. Dursun, C. Shen, M. R. Parida, J. Pan, S. P. Sarmah, D. Priante, N. Alyami, J. Liu, M. I. Saidaminov, M. S. Alias, A. L. Abdelhady, T. K. Ng, O. F. Mohammed, B. S. Ooi, O. M. Bakr, *ACS Photonics* **2016**, *3*, 1150.
[8] M. D. Birowosuto, D. Cortecchia, W. Drozdowski, K. Brylew, W. Lachmanski, A. Bruno, C. Soci, *Sci. Rep.* **2016**, *6*, 37254.
[9] J. Song, J. Li, X. Li, L. Xu, Y. Dong, H. Zeng, *Adv. Mater.* **2015**, *27*, 7162.
[10] T. Guner, M. M. Demir, *Phys. Status Solidi A* **2018**, *215*, 1800120.
[11] Y. Wei, Z. Cheng, J. Lin, *Chem. Soc. Rev.* **2019**, *48*, 310.
[12] Y. Xin, H. Zhao, J. Zhang, *ACS Appl. Mater. Interfaces* **2018**, *10*, 4971.
[13] Z. Li, L. Kong, S. Huang, L. Li, *Angew. Chem., Int. Ed.* **2017**, *56*, 8134.
[14] B. J. Bohn, Y. Tong, M. Gramlich, M. L. Lai, M. Döblinger, K. Wang, R. L. Z. Hoye, P. Müller-Buschbaum, S. D. Stranks, A. S. Urban, L. Polavarapu, J. Feldmann, *Nano Lett.* **2018**, *18*, 5231.
[15] R. S. , V. Nayak, M. S. Jyothi, R. Geetha Balakrishna, *J. Alloys Compd.* **2020**, *834*, 155246.
[16] S. Wang, C. Bi, J. Yuan, L. Zhang, J. Tian, *ACS Energy Lett.* **2017**, *3*, 245.

© 2022 Wiley-VCH GmbH

[17] G. Raino, A. Landuyt, F. Krieg, C. Bernasconi, S. T. Ochsenbein, D. N. Dirin, M. I. Bodnarchuk, M. V. Kovalenko, *Nano Lett.* **2019**, *19*, 3648.
[18] B. Luo, F. Li, K. Xu, Y. Guo, Y. Liu, Z. Xia, J. Z. Zhang, *J. Mater. Chem. C* **2019**, *7*, 2781.
[19] B. Walker, G. H. Kim, J. Y. Kim, *Adv. Mater.* **2019**, 1807029.
[20] C. Shen, Y. Zhao, L. Yuan, L. Ding, Y. Chen, H. Yang, S. Liu, J. Nie, W. Xiang, X. Liang, *Chem. Eng. J.* **2019**, *382*, 122868.
[21] Z. J. Yong, S. Q. Guo, J. P. Ma, J. Y. Zhang, Z. Y. Li, Y. M. Chen, B. B. Zhang, Y. Zhou, J. Shu, J. L. Gu, L. R. Zheng, O. M. Bakr, H. T. Sun, *J. Am. Chem. Soc.* **2018**, *140*, 9942.
[22] J. Y. Woo, Y. Kim, J. Bae, T. G. Kim, J. W. Kim, D. C. Lee, S. Jeong, *Chem. Mater.* **2017**, *29*, 7088.
[23] B. A. Koscher, J. K. Swabeck, N. D. Bronstein, A. P. Alivisatos, *J. Am. Chem. Soc.* **2017**, *139*, 6566.
[24] W. Ke, C. Xiao, C. Wang, B. Saparov, H. S. Duan, D. Zhao, Z. Xiao, P. Schulz, S. P. Harvey, W. Liao, W. Meng, Y. Yu, A. J. Cimaroli, C. S. Jiang, K. Zhu, M. Al-Jassim, G. Fang, D. B. Mitzi, Y. Yan, *Adv. Mater.* **2016**, *28*, 5214.
[25] Q. Jiang, D. Rebollar, J. Gong, E. L. Piacentino, C. Zheng, T. Xu, *Angew. Chem., Int. Ed. Engl.* **2015**, *54*, 7617.
[26] S. Thapa, G. C. Adhikari, H. Zhu, P. Zhu, *J. Alloys Compd.* **2021**, *860*, 158501.
[27] J. Y. Woo, J. H. Ko, J. H. Song, K. Kim, H. Choi, Y. H. Kim, D. C. Lee, S. Jeong, *J. Am. Chem. Soc.* **2014**, *136*, 8883.
[28] S. Thapa, G. C. Adhikari, H. Zhu, A. Grigoriev, P. Zhu, *Sci. Rep.* **2019**, *9*, 18636.
[29] N. Phung, R. Félix, D. Meggiolaro, A. Al-Ashouri, G. S. e Silva, C. Hartmann, J. Hidalgo, H. Köbler, E. Mosconi, B. Lai, R. Gunder, M. Li, Z.-K. Wang, K.-l. Wang, K. Nie, E. Handick, R. G. Wilks, J. A. Marquez, B. Rech, T. Unold, J.-P. Correa-Baena, S. Albrecht, F. D. Angelis, M. Bär, A. Abate, *J. Am. Chem. Soc.* **2020**, *142*, 2364.
[30] J. T.-W. Wang, Z. Wang, S. Pathak, W. Zhang, D. W. deQuilettes, F. Wisnivesky-Rocca-Rivarola, J. Huang, P. K. Nayak, J. B. Patel, H. A. Mohd Yusof, Y. Vaynzof, R. Zhu, I. Ramirez, J. Zhang, C. Ducati, C. Grovenor, M. B. Johnston, D. S. Ginger, R. J. Nicholas, H. J. Snaith, *Energy Environ. Sci.* **2016**, *9*, 2892.
[31] W. Travis, E. N. K. Glover, H. Bronstein, D. O. Scanlon, R. G. Palgrave, *Chem. Sci.* **2016**, *7*, 4548.
[32] F. Haque, M. Wright, M. A. Mahmud, H. Yi, D. Wang, L. Duan, C. Xu, M. B. Upama, A. Uddin, *ACS Omega* **2018**, *3*, 11937.
[33] J. Bahadur, A. H. Ghahremani, S. Gupta, T. Druffel, M. K. Sunkara, K. Pal, *Sol. Energy* **2019**, *190*, 396.
[34] I. Robinson, R. Harder, *Nat. Mater.* **2009**, *8*, 291.
[35] J. Pan, L. N. Quan, Y. Zhao, W. Peng, B. Murali, S. P. Sarmah, M. Yuan, L. Sinatra, N. M. Alyami, J. Liu, E. Yassitepe, Z. Yang, O. Voznyy, R. Comin, M. N. Hedhili, O. F. Mohammed, Z. H. Lu, D. H. Kim, E. H. Sargent, O. M. Bakr, *Adv. Mater.* **2016**, *28*, 8718.
[36] C. Wehrenfennig, M. Liu, H. J. Snaith, M. B. Johnston, L. M. Herz, *J. Phys. Chem. Lett.* **2014**, *5*, 1300.
[37] S. De Wolf, J. Holovsky, S. J. Moon, P. Loper, B. Niesen, M. Ledinsky, F. J. Haug, J. H. Yum, C. Ballif, *J. Phys. Chem. Lett.* **2014**, *5*, 1035.
[38] X. Zhang, X. Bai, H. Wu, X. Zhang, C. Sun, Y. Zhang, W. Zhang, W. Zheng, W. W. Yu, A. L. Rogach, *Angew. Chem., Int. Ed. Engl.* **2018**, *57*, 3337.
[39] F. Fang, W. Chen, Y. Li, H. Liu, M. Mei, R. Zhang, J. Hao, M. Mikita, W. Cao, R. Pan, K. Wang, X. W. Sun, *Adv. Funct. Mater.* **2018**, *28*, 1706000.
[40] Solid-State Lighting Technology Fact Sheet-LED Color Characteristics, DOE, **2016**.
[41] P. Zhu, H. Zhu, G. C. Adhikari, S. Thapa, *OSA Continuum* **2019**, *2*, 1880.
[42] S.-D. Lei, B.-J. Liu, Y. Gao, X.-Y. Dong, Y.-J. Gong, J. Xu, Y.-X. Xu, D. Wang, Z.-Q. Guo, T.-Z. Wu, C.-L. Zhou, Z.-J. Cai, Y.-J. Lu, Z. Chen, *IEEE Photonics J.* **2020**, *12*, 8200509.
[43] Z. Guo, K. Liu, L. Zheng, T.-m. Shih, Y. Lu, T. Wu, Y. Lin, Y. Zhang, J. Zheng, J. Chen, L. Chen, Z. Chen, *IEEE Photonics J.* **2019**, *11*, 8200110.
[44] S. Thapa, G. C. Adhikari, H. Zhu, P. Zhu, *J. Opt. Soc. Am. B* **2019**, *36*, 1616.
[45] X. Di, L. Shen, J. Jiang, M. He, Y. Cheng, L. Zhou, X. Liang, W. Xiang, *J. Alloys Compd.* **2017**, *729*, 526.
[46] C. Yu, Z. Chen, J. J. Wang, W. Pfenninger, N. Vockic, J. T. Kenney, K. Shum, *J. Appl. Phys.* **2011**, *110*, 063526.

 © 2022 Wiley-VCH GmbH